


# NSE5 subunit interacts with distant regions of the SMC arms in the *Physcomitrium patens* SMC5/6 complex

Jitka Vaculíková<sup>1</sup>, Marcela Holá<sup>2</sup>, Barbora Králová<sup>1</sup>, Edit Lelkes<sup>1</sup>, Barbora Štefanovic<sup>1,3</sup>, Radka Vágnerová<sup>2</sup>, Karel J. Angelis<sup>2,\*</sup> and Jan J. Paleček<sup>1,3,\*</sup> 

<sup>1</sup>National Centre for Biomolecular Research, Faculty of Science, Masaryk University, Kamenice 5, 62500 Brno, Czech Republic,

<sup>2</sup>Institute of Experimental Botany Czech Academy of Sciences, Na Karlovce 1, 16000 Prague, Czech Republic, and

<sup>3</sup>Mendel Centre for Plant Genomics and Proteomics, Central European Institute of Technology, Masaryk University, Kamenice 5, 62500 Brno, Czech Republic

Received 13 January 2024; revised 21 May 2024; accepted 25 May 2024; published online 10 June 2024.

\*For correspondence (e-mail [jpalecek@sci.muni.cz](mailto:jpalecek@sci.muni.cz); [karel.angelis@gmail.com](mailto:karel.angelis@gmail.com)).

## SUMMARY

Structural maintenance of chromosome (SMC) complexes play roles in cohesion, condensation, replication, transcription, and DNA repair. Their cores are composed of SMC proteins with a unique structure consisting of an ATPase head, long arm, and hinge. SMC complexes form long rod-like structures, which can change to ring-like and elbow-bent conformations upon binding ATP, DNA, and other regulatory factors. These SMC dynamic conformational changes are involved in their loading, translocation, and DNA loop extrusion. Here, we examined the binding and role of the PpNSE5 regulatory factor of *Physcomitrium patens* PpSMC5/6 complex. We found that the PpNSE5 C-terminal half (aa230–505) is required for binding to its PpNSE6 partner, while the N-terminal half (aa1–230) binds PpSMC subunits. Specifically, the first 71 amino acids of PpNSE5 were required for binding to PpSMC6. Interestingly, the PpNSE5 binding required the PpSMC6 head-proximal joint region and PpSMC5 hinge-proximal arm, suggesting a long distance between binding sites on PpSMC5 and PpSMC6 arms. Therefore, we hypothesize that PpNSE5 either links two antiparallel SMC5/6 complexes or binds one SMC5/6 in elbow-bent conformation, the later model being consistent with the role of NSE5/NSE6 dimer as SMC5/6 loading factor to DNA lesions. In addition, we generated the *P. patens* *Ppnse5KO1* mutant line with an N-terminally truncated version of PpNSE5, which exhibited DNA repair defects while keeping a normal number of rDNA repeats. As the first 71 amino acids of PpNSE5 are required for PpSMC6 binding, our results suggest the role of PpNSE5–PpSMC6 interaction in SMC5/6 loading to DNA lesions.

**Keywords:** *Physcomitrium patens* SMC5/6 complex, NSE5/SNI1/SLF1/SIMC1, NSE6/ASAP1/SLF2/KRE29, DNA damage repair, rDNA stability, moss caulonemata development.

## INTRODUCTION

Structural maintenance of chromosome (SMC) complexes are molecular machines that organize chromatin and regulate its dynamics (Davidson & Peters, 2021; Uhlmann, 2016). Best characterized are the eukaryotic cohesin and condensin that organize chromosomal DNAs into loops during interphase and mitosis, respectively. Although the SMC5/6 complex can also extrude loops (Pradhan et al., 2023), its function(s) is less understood. SMC5/6 was implicated in DNA repair, replication fork restart, rDNA repeat stability maintenance, segregation, transcription, and viral restriction, but the interrelations between these functions are unclear (Aragón, 2018; Paleček, 2019).

The core of the SMC complexes is formed by two SMC proteins, kleisin, and kleisin-associated subunits (Hassler et al., 2018). The SMC proteins fold into a unique structure consisting of an ATPase head at one end and a long coiled-coil arm separating the head from the hinge at the other. The hinge domains dimerize SMC molecules, and arms closely align from hinge to head in a “zipped-up” conformation, resulting in a rod-like structure tens of nanometers long. Upon ATP binding to ATPase heads, the arms “unzip” and adopt ring-shaped conformation. The other core subunits, kleisin (NSE4), and kleisin-associated (KITE: NSE1 and NSE3), bind DNA and regulate the rod-to-ring SMC5–SMC6 dynamics (Paleček &

Gruber, 2015; Vondrova et al., 2020; Yu et al., 2022; Zabrady et al., 2016). These rod-to-ring arm transitions of SMC complexes are possible via discontinuities in their coiled-coil structure. The discontinuities also allow a sharp bending of arms at “elbows,” bringing hinges close to the head area (Lee et al., 2020; Petela et al., 2021). Such bending and the opening of the hinges are considered key steps in the DNA loading; for example, cohesin bending positions head-proximal Scc2 loading factor close to SMC hinges (Collier et al., 2020; Collier & Nasmyth, 2022; Higashi et al., 2021; Shi et al., 2020). Upon SMC complex loading, the ATP binding and hydrolysis drive complex translocation along DNA or loop extrusion (Davidson et al., 2019; Ganji et al., 2018; Pradhan et al., 2023). Interestingly, SMC5/6 translocates as a monomer, while loop extrusion requires dimerization of complex.

Multiple functions of the SMC5/6 complexes are facilitated by various factors (Mahrik et al., 2023), of which the NSE5–NSE6 dimer is the best characterized at the molecular level (Oravcová & Boddy, 2019). Yeast NSE5–NSE6 dimers interact with BRCT domain-containing proteins Brc1/Rtt107, which in turn bind to damage-induced phosphorylated H2A and load SMC5/6 at DNA lesions (Li et al., 2012; Williams et al., 2010). In humans, NSE5A/SLF1 ortholog contains the BRCT domain, which recognizes damage-induced phosphorylation of RAD18 and targets SMC5/6 to DNA lesions (Räschle et al., 2015). Another human NSE5B/SIMC1 ortholog contains SUMO interacting motifs (SIMs), which bind SUMOylated proteins in viral replication centres and facilitate SMC5/6 role in viral restriction (Oravcova et al., 2022). Despite very low sequence similarities between yeast and human NSE5 factors, they share some common features (particularly, they dimerize with NSE6 and directly or indirectly associate with SMC5–SMC6 subunits). The way they associate with SMC5–SMC6 proteins is somehow divergent (Gutierrez-Escribano et al., 2020; Palecek et al., 2006; Taschner et al., 2021; Yu et al., 2021). So far no direct binding of human NSE5 orthologs to SMC proteins was found (Adamus et al., 2020; Oravcova et al., 2022), and reports on yeast orthologs caused controversy. Cross-linking studies placed yeast ScNSE5 primarily to SMC head-proximal areas (Gutierrez-Escribano et al., 2020; Taschner et al., 2021; Yu et al., 2021), while pull-down experiments suggested its association with SMC hinges (Duan et al., 2009).

To bring new insight into this controversy and NSE5 features, we analyzed PpNSE5 interactions with PpNSE6 and PpSMC subunits of *Physcomitrium patens*. We found PpSMC5 hinge-proximal and PpSMC6 head-proximal regions, which are tens of nanometers apart in SMC5/6 rod-like structure, essential for PpNSE5 binding. To interpret these findings, we proposed that NSE5–NSE6 dimers either bridge these regions between two antiparallel

SMC5/6 complexes or bind them when they are next to each other within the elbow-bent SMC5/6 structure. To analyze the role of PpNSE5 binding to PpSMC6, we generated the *P. patens* mutant line (KO1) carrying a truncated version of PpNSE5, missing amino acids specifically required for PpSMC6 binding. This *PpNSE5KO1* mutant line exhibited DNA repair defects with the rDNA number of repeats unaffected, suggesting the specific role of PpNSE5–PpSMC6 interaction in DNA repair.

## RESULTS

### *Physcomitrium patens* PpNSE5 region aa230–505 is essential for binding to PpNSE6

Recently, we characterized the moss PpNSE6 subunit of SMC5/6 and its binding to the PpNSE5 partner (Lelkes et al., 2023). Here, we complemented this analysis with a study of the binding properties of PpNSE5. First, we cloned its N- and C-terminally truncated PpNSE5 fragments to yeast 2-hybrid (Y2H) vectors (Figure 1a). We found Gal4BD–PpNSE5(aa190–526) and (aa230–526) fragments binding to full-length (FL) Gal4AD–PpNSE6(aa1–480), while Gal4BD–PpNSE5(aa265–526) was unable to bind (Figure 1b, lanes 1–4). Similarly, Gal4BD–PpNSE5(aa1–505) was able to bind PpNSE6, while fragments aa1–485 and aa1–455 could not (Figure 1b, lanes 5–7). Notably, the binding of PpNSE5 (aa230–526) and (aa1–505) fragments was weaker than FL PpNSE5 (Figure 1b, compare 0.2 mM AT middle and 5 mM AT bottom panels). These results suggest the essential role of the C-terminal half (aa230–505) and the stabilizing effect of N- (aa190–230) and C-terminal (aa505–526) flanking sequences.

As our STOP-codon CRISPR/Cas9 strategy produced an N-terminally truncated PpNSE5 fragment translated from an alternative start site (see below), we also prepared fragments starting from native methionines (Met72, Met109, Met245, and Met284; Figure 1a). The Gal4BD–PpNSE5(aa72–526) and (aa109–526) fragments bound FL PpNSE6 with an affinity similar to FL PpNSE5, while the PpNSE5(aa245–526) and PpNSE5(aa284–526) fragments lost the binding completely (Figure 1c, lanes 1–4). These data confirm the above conclusion that the N-terminal part of PpNSE5 is dispensable, while amino acids from position aa230 are essential for the PpNSE5–PpNSE6 interaction.

To verify our Y2H results, we expressed the PpNSE5 (aa190–526) and PpNSE5(aa245–526) fragments *in vitro* and used them in a pull-down assay (Figure 1d; Lelkes et al., 2023). The Stag–PpNSE6(aa1–370) specifically precipitated PpNSE5(aa190–526), while not precipitating PpNSE5 (aa245–526) (Figure 1d, lanes 3 and 9), thus confirming the Y2H results. Altogether, our results suggested the essential role of the C-terminal part (aa230–505) of PpNSE5 in PpNSE6 binding.

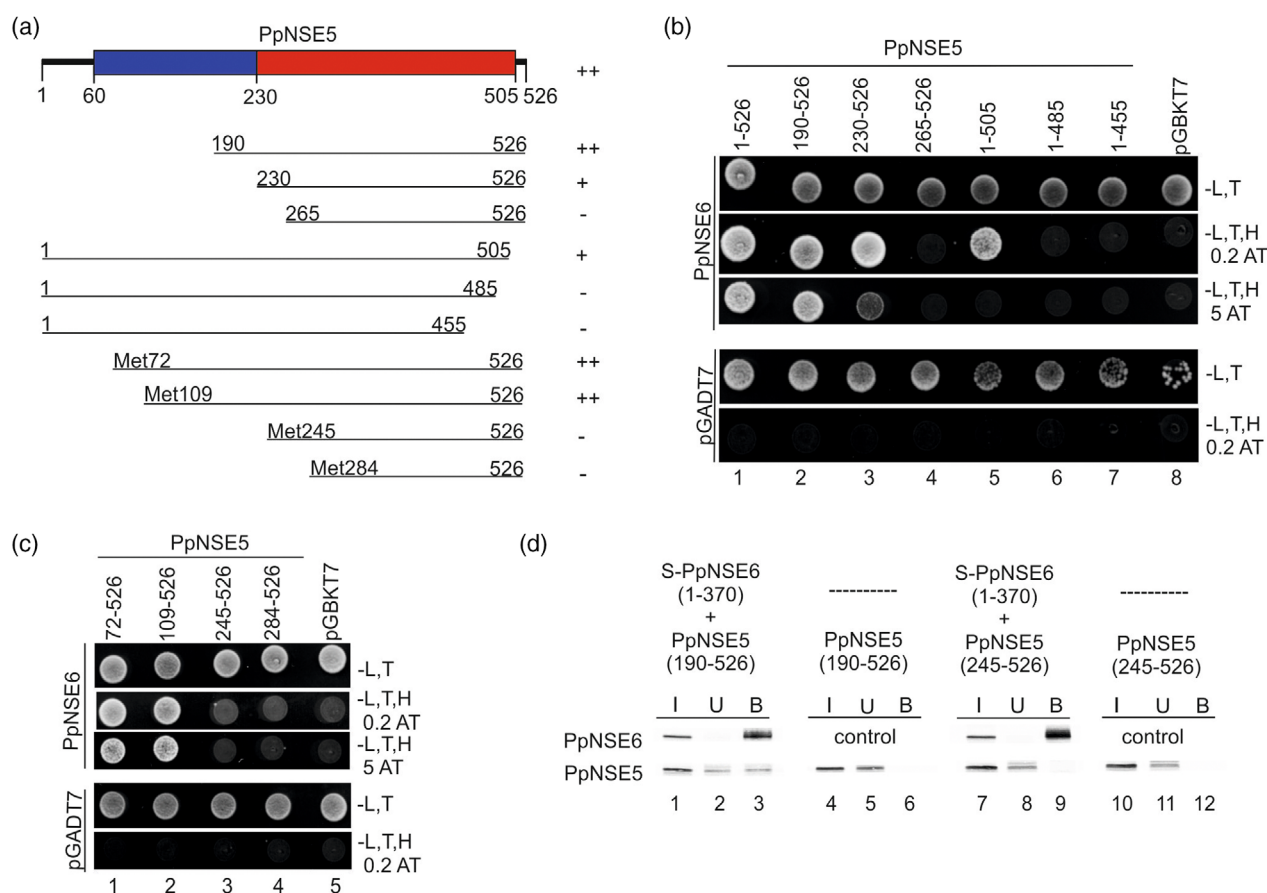


**Figure 1.** Analysis of the PpNSE5–PpNSE6 interaction.

(a) Schematic representation of the different PpNSE5 fragments. The unstructured N-terminal part (aa1–60) is shown as a black line; two parts of the structured region are colored in blue (aa60–230) and red (aa230–505), respectively (Figure S1a). The PpNSE5 fragments borders were designed based on secondary and tertiary structure predictions (Figure S1a) or the positions of native methionines. The summary of Y2H results (from panels b and c) is on the right: ++, strong interaction; +, weak interaction; –, no interaction.

(b) The binding of N- and C-terminally truncated Gal4BD-PpNSE5 constructs to Gal4AD-PpNSE6 (aa1–480) was tested in Y2H. Only FL PpNSE5 and PpNSE5 (aa190–526) constructs strongly bound PpNSE6 (lanes 1 and 2, lower panel, growth on 5 mM AT plate), while binding of PpNSE5(aa230–526) and (aa1–505) was weaker (lanes 3 and 5, middle panel, growth on 0.2 mM AT plate only). PpNSE5(aa265–526), (aa1–485), and (aa1–455) fragments did not bind PpNSE6 (lanes 4, 6, and 7), suggesting the essential role of aa230–505 for PpNSE5–PpNSE6 interaction.

(c) Fragments starting from native methionines Gal4BD-PpNSE5(aa72–526) and (aa109–526) strongly bound Gal4AD-PpNSE6(aa1–480), while Gal4BD-PpNSE5(aa245–526) and Gal4BD-PpNSE5(aa284–526) did not. All Y2H protein–protein interactions were scored by the growth of the yeast PJ69-4a transformants on the plates without Leu, Trp, His (–L,T,H), and with the indicated concentration of 3-Amino-1,2,4-triazole (AT). Control plates were lacking only Leu and Trp (–L,T). Empty pGBKT7 and pGADT7 vectors were used as negative controls.

(d) The Y2H results were verified using *in vitro* pull-down assays. The plasmids pGBKT7-PpNSE5(aa190–526), pGBKT7-PpNSE5(aa245–526), and pET-Duet-PpNSE6(aa1–370)-StrepTwin-Stag were used for *in vitro* expression, radiolabeled proteins were mixed (as indicated), and added to the protein-S beads. In the control experiments, PpNSE5 proteins were applied to empty beads. The input (I), unbound (U), and bound (B) fractions were separated on 12% SDS-PAGE and transferred to nitrocellulose membranes. The blots were scanned for autoradiography.

### The first 71 amino acids of PpNSE5 are required for binding to PpSMC6

Yeast NSE5 subunits bind directly to SMC arms (Li et al., 2023; Palecek et al., 2006), while there is no evidence for the direct binding of human HsNSE5 orthologs (HsNSE5A/SLF1 or HsNSE5B/SIMC1) to SMC subunits (Adamus et al., 2020; Oravcova et al., 2022). Therefore, we tested the above Y2H constructs (Figure 1a) and other PpNSE5 fragments (Figure 2) against PpSMC5 and PpSMC6 constructs (Lelkes et al., 2023). Surprisingly, only

Gal4AD-PpNSE5(aa1–230) bound PpSMC5 and PpSMC6 (Figure 2a). To verify this unexpected result, we used FL His-T7tag-PpNSE5(aa1–526) and His-T7tag-PpNSE5(aa1–230) proteins in the pull-down assay against PpSMC5 and PpSMC6 constructs (see below). His-T7tag-PpNSE5 proteins were expressed in bacteria, prebound on anti-T7tag agarose beads, and then either PpSMC5 or PpSMC6 *in vitro* expressed proteins were added. Both PpNSE5 proteins bound PpSMC5 (Figure 2b, top panels, lanes 3 and 6), suggesting a false negative result of FL PpNSE5(aa1–526)

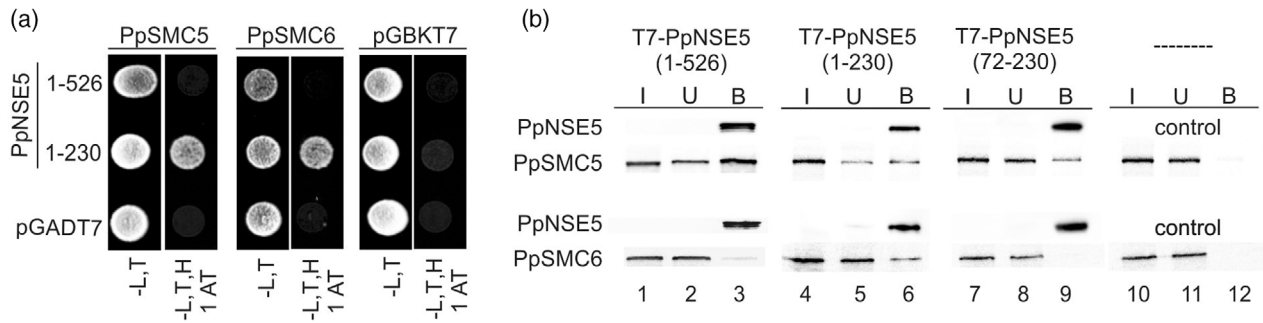


**Figure 2.** Analysis of PpNSE5 binding to SMC subunits.

(a) The Gal4AD-PpNSE5 fragments were tested in Y2H for protein–protein interactions with Gal4BD-PpSMC5(aa201–890) (left panel) and Gal4BD-PpSMC6(aa226–955) (middle panel). Only the N-terminal PpNSE5(aa1–230) fragment bound PpSMC5 and PpSMC6.

(b) The PpNSE5 interactions were further analyzed using *in vitro* pull-down assays. His-T7tag-PpNSE5(aa1–526), His-T7tag-PpNSE5(aa1–230), His-T7tag-PpNSE5(aa72–230) constructs and pET-28c(+) empty vector were expressed in bacteria, prebound on anti-T7tag agarose beads, and then *in vitro* radiolabeled PpSMC5(aa201–890) or PpSMC6(aa226–510 + 654–955) protein was applied. While PpNSE5(aa1–230) bound both PpSMC subunits (lane 6), PpNSE5(aa72–230) bound only PpSMC5 but not PpSMC6 (lane 9), suggesting the essential role of the first 71 amino acids for PpNSE5–PpSMC6 interaction. The bacterially expressed His-T7tag-PpNSE5 bait proteins were analyzed using the anti-T7 antibody. The other details of pull-down and Y2H assays are as in Figure 1.

Y2H construct in combination with PpSMC5. Consistent with Y2H results, only PpNSE5(aa1–230) protein was able to pull down PpSMC6 (Figure 2b, bottom panels, lane 6), while FL PpNSE5(aa1–526) was not (Figure 2b, bottom panels, lane 3), suggesting a complex binding mechanism between PpNSE5 and PpSMC6.

To see whether the PpNSE5 alternative Met72 start could affect these interactions, we also prepared His-T7tag-PpNSE5(aa72–230) construct and tested its binding to PpSMC5 and PpSMC6 in the pull-down assay (Figure 2b). Interestingly, this PpNSE5(aa72–230) fragment was able to interact with PpSMC5, but not with the PpSMC6 subunit (lane 9), suggesting that N-terminal 71 amino acids are essential for interaction with PpSMC6 but not PpSMC5.

### PpSMC6 joint region is required for PpNSE5 and PpNSE6 binding

To analyze PpNSE5–PpSMC6 interaction further, we prepared different arm fragments of PpSMC6 truncated from the head- or hinge-proximal end (Figure 3a; Lelkes et al., 2023). The long headless fragments Gal4BD-PpSMC6(aa226–955) and (aa255–923) bound both Gal4AD-PpNSE5(aa1–230) and Gal4AD-PpNSE6(aa1–370) (Figure 3b, lanes 1 and 2). In contrast, the shorter headless fragment Gal4BD-PpSMC6(aa290–870) failed to interact with PpNSE5 and PpNSE6 subunits (Figure 3b, lane 3). Notably, these fragments showed the functional ability to bind the PpSMC5(aa360–710) fragment containing the hinge region

**Figure 3.** Detailed analysis of PpSMC5 and PpSMC6 interactions with PpNSE5.

(a) Schematic representation of the PpSMC6 polypeptide chain, containing N- and C-terminal parts of the head domain, N- and C-terminal helical segments of the arm, and the hinge domain. The polypeptide folds back at the hinge domain, and its N-/C-terminal parts assemble to the coiled-coil arm and ATPase head (vertical scheme on the right). Y2H results from PpSMC6 binding analysis to PpNSE5 and PpNSE6 (panel b) are summarized on the left: +, binding; –, not binding.

(b) Gal4BD-PpSMC6 constructs (depicted in panel a) were analyzed for their binding to Gal4AD-PpNSE5(aa1–230) (top panels) and Gal4AD-PpNSE6(aa1–370) (middle panels). The Gal4BD-PpSMC6(aa226–955) and (aa255–923) fragments were able to bind PpNSE5 and PpNSE6 constructs, while the Gal4BD-PpSMC6(aa290–870) fragment was not (lanes 1–3), suggesting an essential role of the joint region for these interactions. Similarly, Gal4BD-PpSMC6(aa226–510 + 654–955) and Gal4BD-PpSMC6(aa226–405 + 750–955) constructs bound both PpNSE5 and PpNSE6 fragments, while the Gal4BD-PpSMC6(aa226–310 + 836–955) construct did not.

(c) The PpNSE5 interactions with selected PpSMC6 arm constructs were verified using *in vitro* pull-down assays.

(d) Schematic representation of the different PpSMC5 constructs (the PpSMC5 polypeptide folds similarly to PpSMC6; panel a). Y2H results from PpNSE5 and PpNSE6 binding analyses are summarized on the right: +, binding; –, not binding.

(e) Detailed mapping of PpSMC5 binding to PpNSE5. The Gal4AD-PpNSE5(aa1–230) and Gal4AD-PpNSE6(aa1–370) constructs bound Gal4BD-PpSMC5(aa280–790) headless construct but not its N- and C-terminally truncated versions, suggesting PpNSE5 binding similar to PpNSE6 (lanes 1–5). However, the PpNSE5 binding pattern with PpSMC5 hingeless constructs was different (lanes 6–8), suggesting that PpNSE5 occupies the hinge-proximal half of the PpSMC5 arm (aa280–430 and aa630–775), while PpNSE6 binds only its middle part (aa280–350 and 695–765).

(f) The PpNSE5 interactions with PpSMC5(aa280–430 + 630–775) and (aa280–380 + 685–775) arm constructs were verified using *in vitro* pull-down assays. All protein–protein interactions were scored in the same way as in Figure 1.

(g) Summary of protein–protein interaction mapping. Arrows delineate the PpSMC5 and PpSMC6 areas (defined by Y2H fragment analysis), which are essential for interactions with PpNSE5 (red) and PpNSE6 (orange).



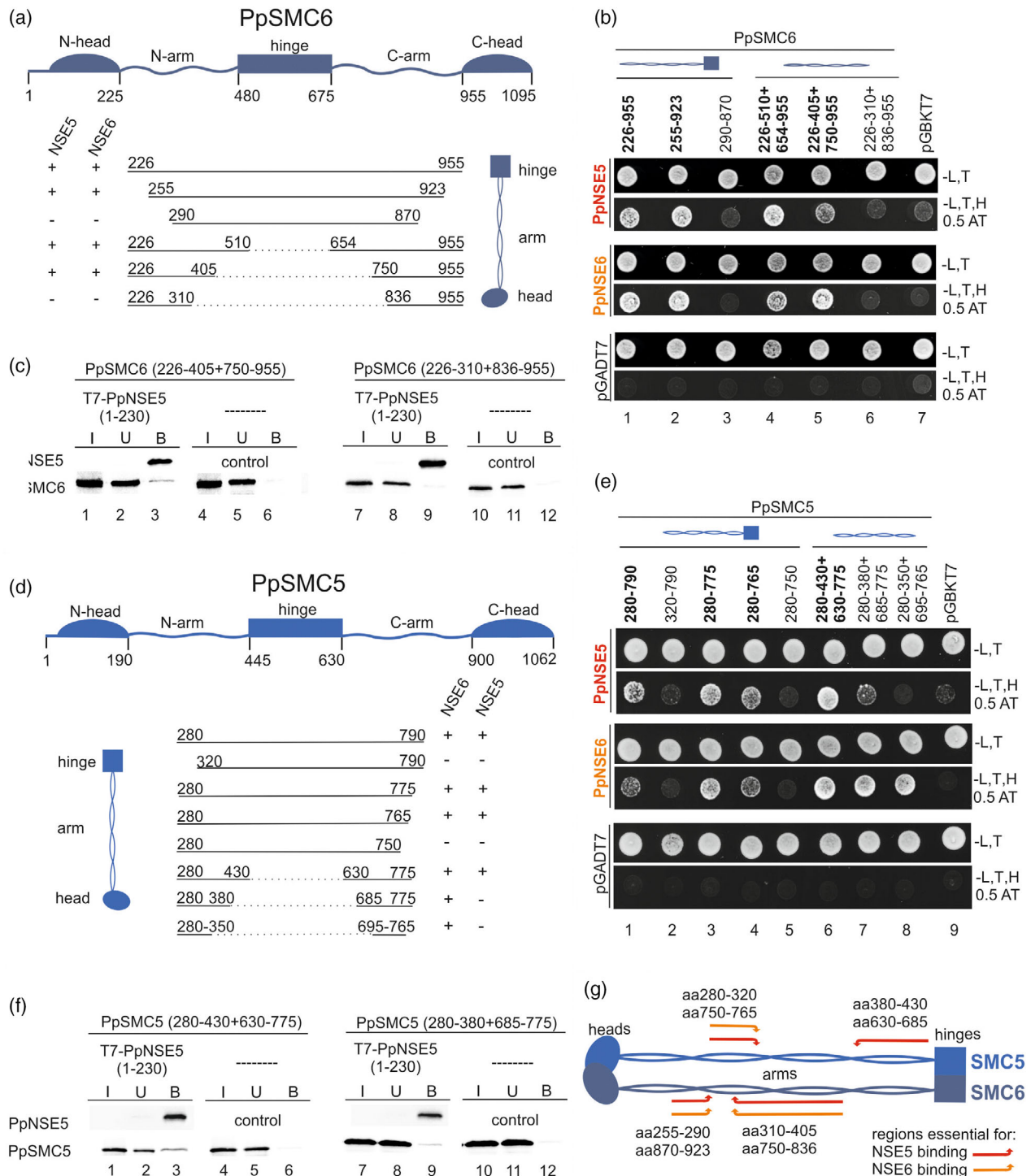


(Figure S2a; Alt et al., 2017; Sergeant et al., 2005). These data suggest the essential role of the PpSMC6 joint region (aa255–290 and aa870–923) for PpNSE5 and PpNSE6 binding.

Next, we prepared PpSMC6 arm-only constructs, missing both hinge and head domains, and tested them

for binding to the PpNSE5 and PpNSE6 subunits. The long constructs Gal4BD-PpSMC6(aa226–510 + 654–955) and (aa226–405 + 750–955) bound both PpNSE subunits (Figure 3b, lanes 4 and 5), suggesting no role of head and hinge domains in PpSMC6 binding to PpNSE partners. In contrast, the shortest arm construct (aa226–310 + 836–955)

was not able to bind PpNSE5 or PpNSE6 (Figure 3b, lane 6). To confirm later Y2H results, we used His-T7tag-PpNSE5(aa1–230) protein in the pull-down assay against the above PpSMC6 arm constructs. Consistently, we detected weak PpNSE5 interactions with PpSMC6(aa226–510 + 654–955) and (aa226–405 + 750–955), but not with (aa226–310 + 836–955) construct (Figures 2b and 3c). Altogether, PpNSE5 requires PpSMC6 sequences within aa310–405 and aa750–836 and joint region.

### The hinge-proximal part of the PpSMC5 arm is essential for PpNSE5 binding

Like with PpSMC6, we wanted to delineate the PpNSE5-binding region of PpSMC5 and used a similarly designed panel of constructs (Figure 3d; Lelkes et al., 2023). We found that the Gal4BD-PpSMC5(aa280–790) headless fragment interacts with both Gal4AD-PpNSE5 and Gal4AD-PpNSE6 (Figure 3e, lane 1). These interactions were abrogated by 40 amino acid truncations either from N- or C-terminus (fragments aa320–790 and aa280–750; Figure 3e, lanes 2 and 5), suggesting PpNSE5 binding similar to PpNSE6 (as well as to PpNSE2; Figure S3a; Lelkes et al., 2023). However, when we employed PpSMC5 hingeless constructs (Figure 3d), we found different binding patterns for PpNSE5 and PpNSE6. While the longest arm construct (aa280–430 + 630–775) interacted with all three partners (PpNSE5, PpNSE6, and PpNSE2; Figure 3e and Figure S3a, lane 6), shorter hingeless constructs (aa280–380 + 685–775 and aa280–350 + 695–765) bound only PpNSE6 and PpNSE2 but not PpNSE5 (Figure 3e and Figure S3a, lanes 7 and 8). Again, we used His-T7tag-PpNSE5(aa1–230) protein in the pull-down assay against the PpSMC5(aa280–430 + 630–775) and (aa280–380 + 685–775) constructs and confirmed Y2H results (Figure 3f). Our results suggest that PpNSE5 requires a hinge-proximal part of the PpSMC5 arm (aa380–430 and aa630–685; summarized in Figure 3g), while PpNSE2 and PpNSE6 occupy only its middle part (aa280–350 and aa695–765).

### Generation and analysis of the moss *PpNSE5* mutants

To characterize the PpNSE5 function, we created two distinct *PpNSE5* moss mutant lines. These mutants involved the insertion of a STOP codon via CRISPR/Cas9

homology-directed repair at either amino acid position 14 (*PpNSE5KO1*) or 168 (*PpNSE5KO2*) within the *PpNSE5* open-reading frame (Figure 4a). We successfully obtained several viable mutant lines, suggesting a non-essential role of the *PpNSE5* gene similar to *PpNSE6* (Lelkes et al., 2023). We selected *PpNSE5KO1-16* and *PpNSE5KO2-14* lines for further analysis. *PpNSE5KO1-16* exhibited a growth rate similar to WT, while the *PpNSE5KO2-14* mutant displayed a growth rate reduction of 37% (Figure S4a). Both mutant lines showed developmental abnormalities (Figure 4b,c) with inhibited gametophore formation. Notably, the gametophores of *PpNSE5KO2-14* were more defective, with fewer phyllids than *PpNSE5KO1-16*.

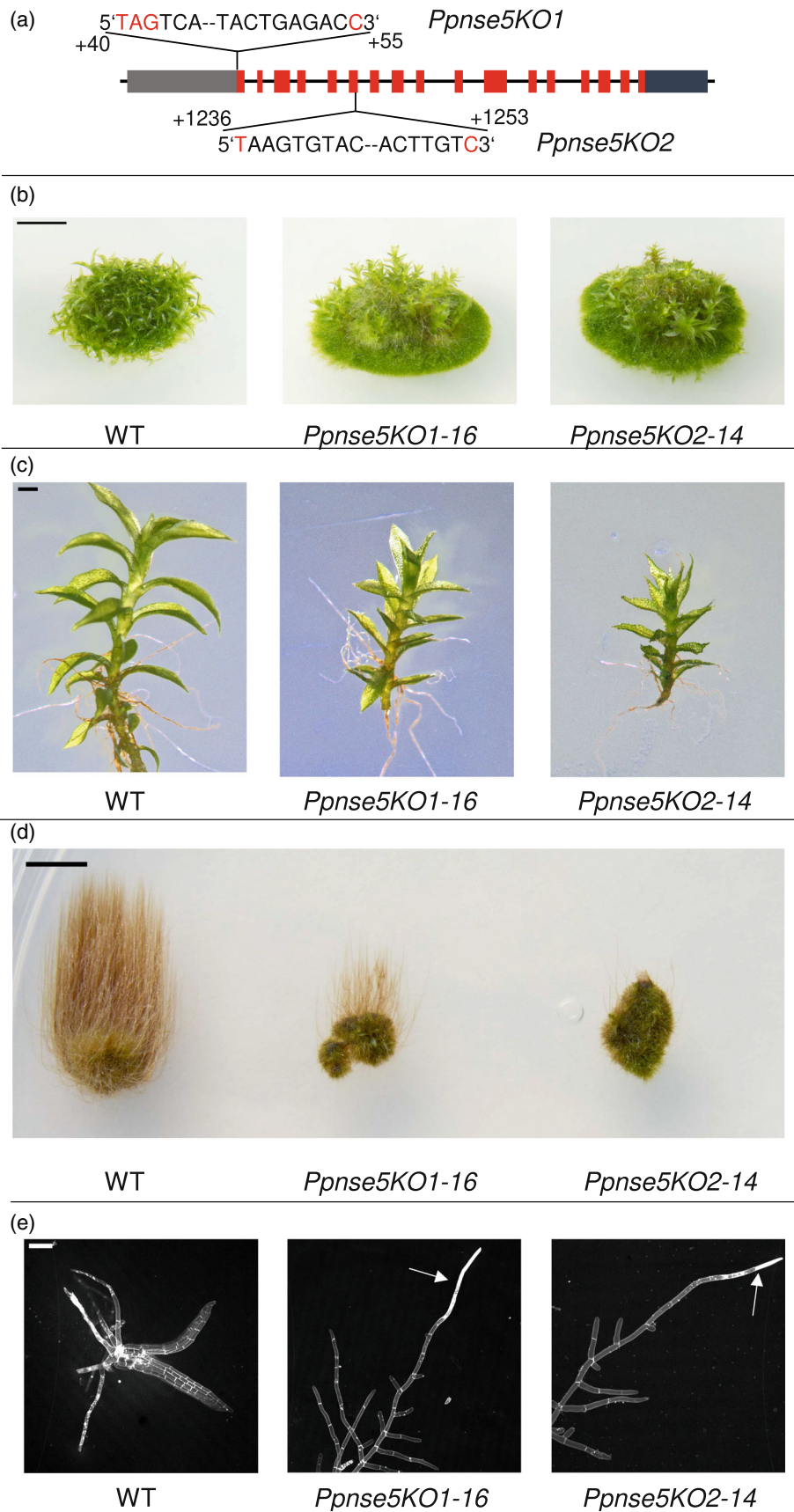
We took advantage of the development of gametophores and caulonemata (but not chloronemata) without light (Cove et al., 1978) and investigated the transition from chloronema to caulonema in mutant lines. After 3 weeks under dark conditions, WT plants produced long, negatively gravitropic caulonemata (Figure 4d). In contrast, both *PpNSE5KO* mutant lines exhibited a severe inhibition in the production of caulonemal filaments. Furthermore, propidium iodide (PI) staining of 10-day-old protonema revealed that the rarely occurring apical caulonemal cells were often defective, displaying premature senescence, and leading to cell death in mutant lines (Figure 4e). Microscopic analysis also showed a marked delay in bud development and, consequently, gametophore formation in both mutant lines. By day 10 after planting, WT plants had already initiated the development of juvenile gametophores. In contrast, the mutant lines had only produced apical caulonemal cells, suggesting the role of PpNSE5 in moss development. Interestingly, the *PpNSE5KO2-14* phenotypes were pronounced more than in *PpNSE5KO1-16* (Figure 4b–d).

### Role of *PpNSE5* in the maintenance of genome stability

Based on the best-known role of SMC5/6 subunits in DNA repair and replication (Aragón, 2018; Palecek, 2019), we determined the growth response of the *PpNSE5* mutant lines to exogenous DNA damage (Holá et al., 2021). As expected, both lines were sensitive to the radiomimetic drug bleomycin, although to a different extent (Figure 5a). After treatment with 30 µg/mL BLM, the growth of WT was decreased to 77% of the weight of

**Figure 4.** Characterization of the moss *PpNSE5* mutant lines.

(a) Schematic representation of exon/intron distribution of *PpNSE5* gene. Detailed positions and sequences of the knock-in mutations introduced by the CRISPR/Cas9 system to generate *PpNSE5KO1* and *PpNSE5KO2* STOP-codons at aa14 and aa168, respectively. (b–d) Representative morphologies of *PpNSE5KO1-16* and *PpNSE5KO2-14* mutant lines suggest developmental defects in *PpNSE5* mutants. (b) 1-month-old colonies of WT and *PpNSE5* mutant lines grown on BCDAT medium. Scale bar = 5 mm. (c) Detail photos of individual gametophores of WT and *PpNSE5* mutant lines. Scale bar = 1 mm. (d) Comparison of caulonema development in WT and mutant lines after 3 weeks under stimulating conditions. Scale bar = 5 mm. (e) 10-day-old protonema stained with propidium iodide. In the WT sample, juvenile gametophores are evident, whereas the *PpNSE5KO1-16* and *PpNSE5KO2-14* mutant lines continue to develop apical caulonemal cells, which frequently exhibit damage (indicated by arrows). Scale bar = 100 µm.



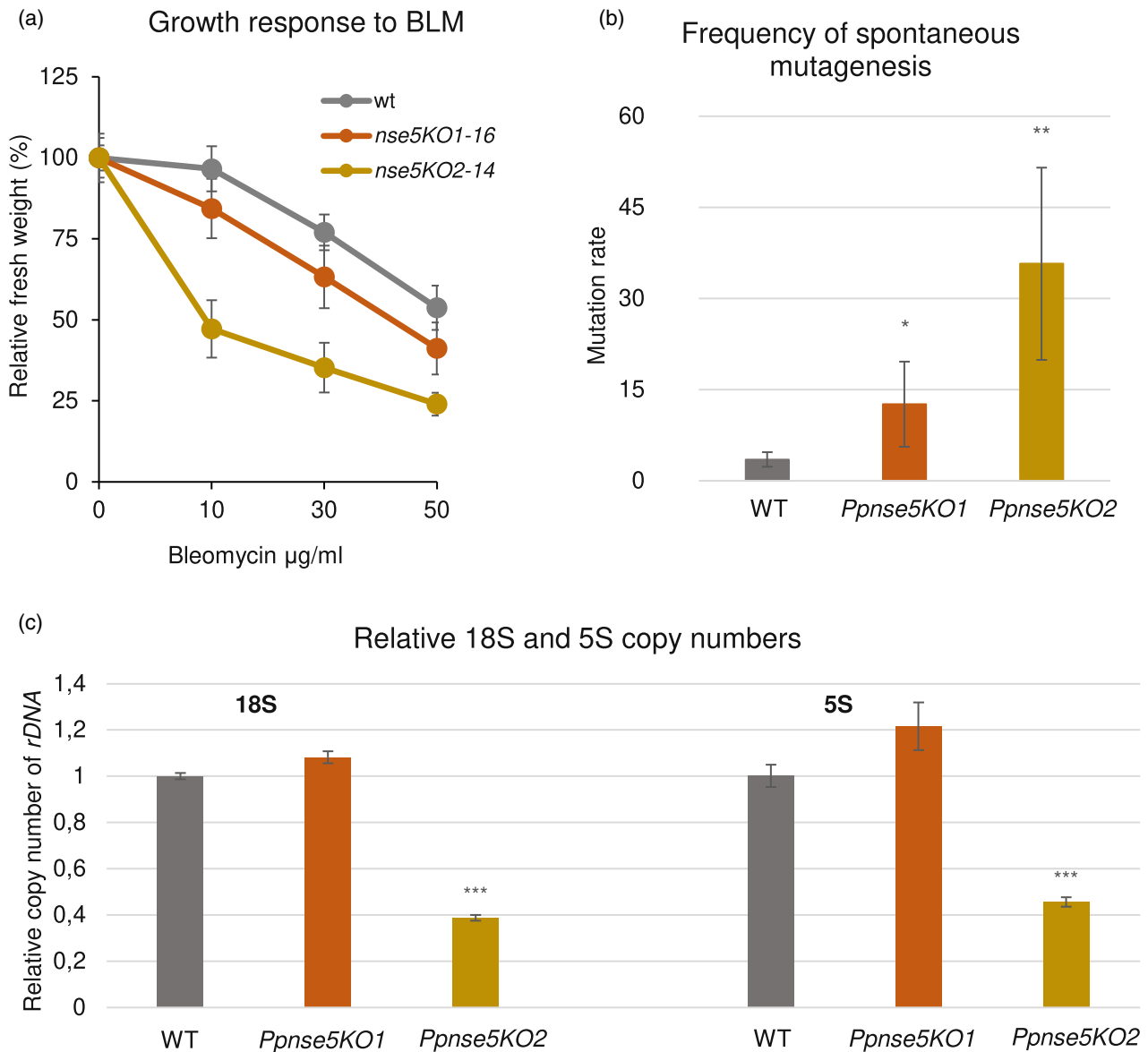


**Figure 5.** Analysis of the genome stability maintenance in *Ppnse5* mutant lines.

(a) The growth response of WT and *Ppnse5* plants treated for 1 h with 10, 30, and 50 µg/mL bleomycin (BLM). The explants were inoculated on a BCDAT medium and grown under standard conditions for 3 weeks. The mean weight of treated explants was normalized to the weight of untreated explants (set as a default 100%). *Ppnse5* mutants exhibited reduced DNA repair efficiency.

(b) The spontaneous mutations in the *APT* gene lead to resistance to 2-FA. The 2-FA surviving colonies were counted and expressed as the number of 2-FA resistant colonies per mg of dry tissue. Spontaneous mutagenesis is increased to 12.6 in *Ppnse5KO1-16* and 35.7 in *Ppnse5KO2-14* versus only 3.5 colonies per mg of the dry tissue in the WT.

(c) The relative number of 18S and 5S rDNA copies was measured by qPCR in WT (default set to 1) *Ppnse5* mutant lines. Surprisingly, the *Ppnse5KO1-16* mutant exhibited WT-like levels of rDNA copies.

Student's *t*-test: \**P* < 0.05; \*\**P* < 0.01; \*\*\**P* < 0.001, and error bars represent SD between the means of biological replicates.

untreated plants, while the growth of *Ppnse5KO1-16* and *Ppnse5KO2-14* was reduced to 63% and 35% of the weight of untreated plants, respectively, suggesting high sensitivity of *Ppnse5KO2-14*.

In addition, we analyzed spontaneous mutagenesis using the reporter system that depends on the inactivation

of the adenine phosphoribosyl transferase (*APT*) gene and leads to resistance to halogenated 2-fluoro adenine (2-FA) base (Trouiller et al., 2006). Spontaneous *APT* mutations manifest as increased numbers of 2-FA resistant plants regenerated from *Ppnse5* mutant lines. While there were 3.5 resistant colonies per mg of dry tissue in the WT, it



increased to 12.6 in *Ppnse5KO1–16* and 35.7 in *Ppnse5KO2–14* (Figure 5b), suggesting a reduced capacity of *Ppnse5* mutant lines to process endogenously induced DNA damage of whatever origin. As for exogenous damage (Figure 5a), the DNA repair efficiency of endogenous damage was reduced more in *Ppnse5KO2–14* than in *Ppnse5KO1–16* (Figure 5b).

Given the role of SMC5/6 in *rDNA* stability maintenance (Lelkes et al., 2023; Peng et al., 2018; Torres-Rosell et al., 2007), we measured changes in the number of *rDNA* copies in genomic DNA of 7-day-old protonemata by qPCR. We found *rDNA* copy levels of *Ppnse5KO2–14* significantly reduced (copy numbers of 18S *rDNA* were reduced to 38% and 5S *rDNA* to 45%; Figure 5c) similar to *Ppnse6KO1–47* mutant line (Lelkes et al., 2023). In contrast, the *Ppnse5KO1–16* mutant exhibited WT-like levels of *rDNA* copies (Figure 5c), suggesting different effects of the STOP codon insertions on different SMC5/6 functions.

The most likely explanation for the milder phenotypes of *Ppnse5KO1–16* is that the STOP codon at amino acid position 14 does not abolish PpNSE5 translation completely. We assumed that PpNSE5 translation might start at the alternative ATG codon (Met72), producing the N-terminally truncated PpNSE5(aa72–526) protein. We introduced the 3xFLAG-tag at the 3'-end of PpNSE5 ORF to test this possibility and analyzed its expression in WT and KO1 lines using the anti-FLAG antibody. We observed a clear band in the WT-FLAG (FL PpNSE5) extract corresponding to its theoretical size of 62 kDa and a lower band of roughly 55 kDa in the extract from *Ppnse5KO1*-FLAG line (Figure S4c, lanes 2 and 3), which corresponds to the PpNSE5(aa72–526)-3xFLAG translation product (theoretical size of 54 kDa). Such PpNSE5(aa72–526) protein should be able to interact with PpNSE6 and PpSMC5 partners (Figures 1c and 2b) and therefore assemble the SMC5/6 complex. However, the inability of the PpNSE5(aa72–526) protein to bind PpSMC6 (Figure 2b) could partially compromise SMC5/6 function and result in relatively mild phenotypes (see Discussion).

## DISCUSSION

Here, we characterized PpNSE5 binding to PpNSE6 and PpSMC subunits of *P. patens* PpSMC5/6 complex. Our analyses showed the binding of PpNSE5 to the head-proximal region of PpSMC6 and the hinge-proximal arm of PpSMC5. Consistent with our PpNSE5–PpSMC6 interaction data, the cross-linking studies of budding yeast ScSMC5/6 suggested the proximity of ScNSE5 to ScSMC5–ScSMC6 heads (Gutierrez-Escribano et al., 2020; Taschner et al., 2021; Yu et al., 2021). However, recent cryoEM structure studies narrowed down the binding site of the yeast ScNSE5–ScNSE6 dimer to ScSMC6 neck (Li et al., 2023), while our analyses localized PpNSE5 (and

PpNSE6) to PpSMC6 join region (Figure 3). As the yeast and plant NSE5 (as well as NSE6) sequences exhibit very low homologies (Lelkes et al., 2023; Oravcova et al., 2022), the (slightly) different NSE5–SMC6 binding modes most likely reflect evolutionary distance between yeast and plants.

Nevertheless, these different binding modes may still serve similar functions, given another interesting comparison between binding sites of NSE5–SMC5 in yeasts and plants. It was previously reported that yeast ScSMC5–ScSMC6 hinge fragments co-purify with ScNSE5–ScNSE6 dimers (Duan et al., 2009). In comparison, our results show the binding of PpNSE5 to the hinge-proximal arm of PpSMC5 (Figure 3). Although the binding modes are again (slightly) different between yeasts and plants, the mapping of SMC5 (hinge/hinge-proximal) and SMC6 (neck/joint) sites suggests binding of NSE5 to very distant regions within the SMC5/6 complexes (Figure 6a). The binding sites at hinge/hinge-proximal and neck/joint regions are tens of nanometers apart in rod-like structures, making it unlikely that the NSE5 molecule could bind both areas within such conformation of the SMC5/6 complex. The data rather suggest that NSE5(-NSE6 dimers) either (1) link antiparallel SMC5/6 dimers or (2) bind SMC5/6 monomers in elbow-bent conformation (Figure 6a).

Interestingly, dimers of SMC5/6 complexes (model 1; Figure 6a) were recently implicated in loop extrusion (Pradhan et al., 2023). However, NSE5–NSE6 subunits rather blocked the formation of productive dimers and inhibited loop extrusion. It is possible that loop extrusion requires parallel SMC5/6 dimers while NSE5–NSE6 drives the formation of antiparallel dimers, which are probably incompatible with the loop extrusion. However, given no experimental evidence of NSE5/NSE6-containing SMC5/6 dimers so far, we favor the elbow-bent model (model 2; Figure 6a). In fact, this model is supported by low-resolution cryoEM structures of ScSMC5/6 (co-purified with ScNSE5–ScNSE6 subunits), showing elbow-bent conformations of the complexes (Gutierrez-Escribano et al., 2020). In addition, our AlphaFold modeling of PpSMC5 and PpSMC6 headless fragments provided the elbow-bent structures (Figure 6b and not shown) reminiscent of cohesin and condensin (Lee et al., 2020; Petela et al., 2021). As the bending of cohesin and condensin complexes plays a key role in their loading to DNA (Bürmann & Löwe, 2023), it is reasonable to assume that the binding of the NSE5–NSE6 dimer to bent SMC5/6 assists with its loading. Indeed, the NSE5–NSE6 dimer is considered the major loading factor of SMC5/6 to DNA lesions (Oravcova & Boddy, 2019).

Our *in vivo* results are consistent with the above NSE5–NSE6 loading function and *in vitro* data. We showed that the first 71 amino acids of PpNSE5 are specifically

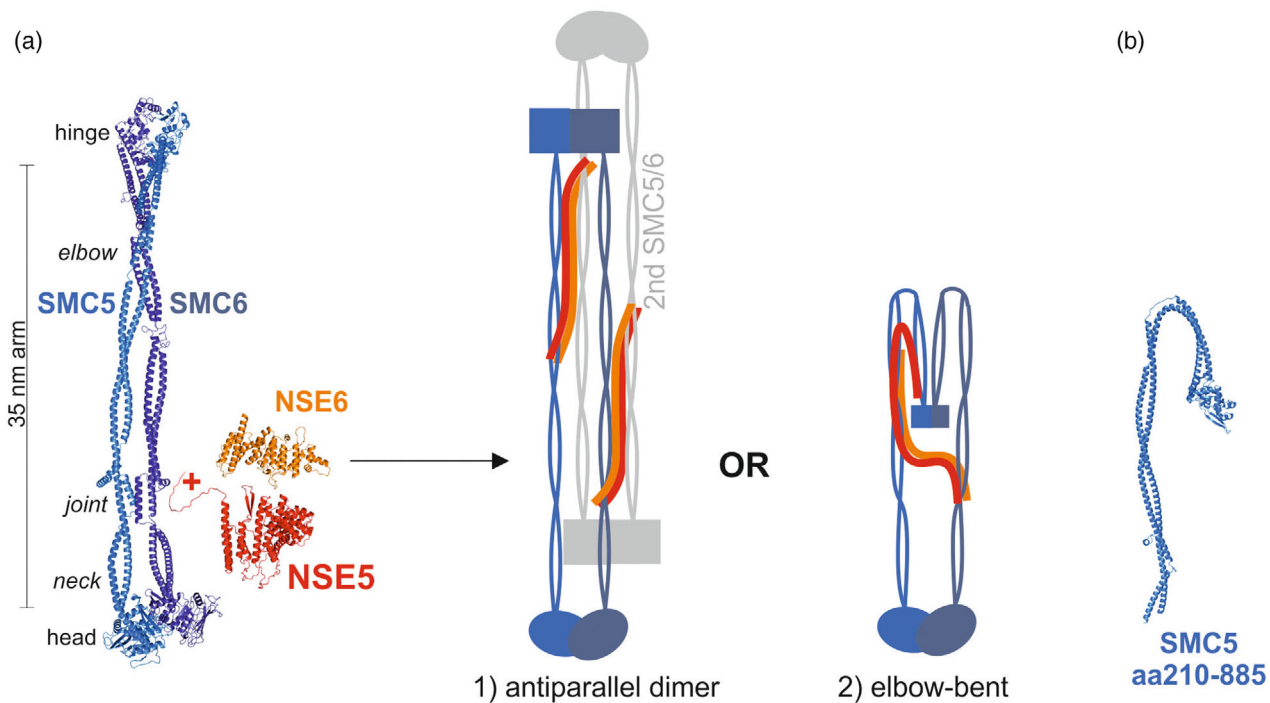


**Figure 6.** Hypothetical models for NSE5/NSE6 binding to distant regions of the SMC arms. (a) Structural rod-like model of PpSMC5-PpSMC6 dimer (based on the 7QCD cryoEM structure; Hallett et al., 2022) compared to the PpNSE5 (red) and PpNSE6 (orange) AlphaFold models. The distance between the head and hinge domains set by the long coiled-coil arm is approximately 35 nm, making it unlikely that mostly globular small NSE5 molecule could bind both the SMC6 joint region and SMC5 hinge-proximal end at the same time. We hypothesize that either (1) the NSE5 molecule binds the SMC6 joint region of the first SMC5-SMC6 dimer (light and dark blue colors, respectively) and SMC5 hinge-proximal end of the second antiparallel SMC5-SMC6 dimer (gray colors) in rod-like conformation or (2) SMC5-SMC6 dimer bends at the elbow and the hinges come closer to the heads, allowing SMC6-joint-bound NSE5 to reach SMC5 hinge-proximal end. The other NSE subunits were omitted for simplicity. (b) The AlphaFold model of the PpSMC5(aa210-885) headless fragment has a bent arm at the elbow region.

required for binding to PpSMC6 while dispensable for interactions with PpNSE6 and PpSMC5 (Figures 1 and 2). Interestingly, the deletion of the first 71 amino acids of PpNSE5 in *P. patens* plants (*PpNSE5K01-16* mutant line) resulted in compromised DNA repair functions (and milder developmental defects; Figure 4) while not affecting rDNA copy numbers (Figure 5). These results suggest that PpNSE5-PpSMC6 interaction is specifically involved in DNA repair-related functions of PpSMC5/6 but not in its replication-coupled activities. This is consistent with NSE5-NSE6 function as the SMC5/6 loader to DNA lesions found in yeasts and humans (Oravcová & Boddy, 2019; Räschele et al., 2015). Strikingly, a recent study showed that yeast mutant cells defective in ScNSE6-ScSMC6 interaction are sensitive to DNA damage but do not exhibit replication-coupled problems (Li et al., 2023).

In conclusion, the binding of NSE5-NSE6 dimer to SMC6 plays a specific role in DNA repair, and this function seems to be conserved (at least from yeast to plants). It will be interesting to reexamine human HsNSE5 binding to HsSMC5 and HsSMC6 subunits (Adamus et al., 2020) and compare their binding sites to yeasts and plants. Altogether, our detailed analysis has already provided new

insights into NSE5 features conserved across species that were previously assumed not to be conserved.

## EXPERIMENTAL PROCEDURES

### Cloning of constructs

For the Y2H constructs, the full-length PpNSE5(aa1-526) construct prepared in Lelkes et al. (2023) was used as a template to create shorter PpNSE5 fragments (Figures 1 and 2). Individual fragments were amplified using specific primers listed in Table S1. PCR products were cloned into the *NdeI-BamHI* sites of pGBKT7 or pGADT7 vectors using NEBuilder (New England BioLabs, USA).

The cloning of pGADT7-PpNSE6 (full length and aa1-370), pGADT7-PpNSE2(aa1-304), pGBKT7-PpSMC5 (containing aa280-790, aa320-790, aa280-775, aa280-765, aa280-750, aa360-710, and aa280-350 + 695-765), and pGBKT7-PpSMC6 (containing aa226-955, aa290-870, and aa226-510 + 654-955) plasmids has been described in Lelkes et al. (2023). The PpSMC6(aa255-923) fragment was amplified using BK005 and BK006 primers (Table S1) and cloned into the *NdeI-BamHI* site of pGBKT7 vector using NEBuilder to obtain Gal4BD-PpSMC6(aa255-923) construct. The Gal4BD-PpSMC5(aa280-430 + 630-775), Gal4BD-PpSMC5(aa280-380 + 685-775), Gal4BD-PpSMC6(aa226-405 + 750-955), and Gal4BD-PpSMC6(aa226-310 + 836-955) hingeless constructs (Figure 3) were cloned in two steps. First, the N-terminal part was amplified by PCR and cloned into the pGBKT7 *NdeI* site. Second, the

C-terminal part was PCR amplified and inserted into the *Bam*HI site of the N-terminal construct created in the first step (Table S1).

For the pull-down assays, pET-Duet-PpNSE6(aa1–370)-StrepTwin-Stag and pET-28a-PpNSE5(aa1–526) plasmids with codon optimized for *Escherichia coli* expression were described in Lelkes et al. (2023). The PpNSE5 fragments aa1–230 and aa72–230 (Figure 2b) were amplified using the primers listed in Table S1. Purified inserts were cloned into the pET-28c(+) vector containing His-T7tag (*Bam*HI-*Xho*I) using NEBuilder.

### Yeast two-hybrid assay

The classical Gal4-based Y2H system was used to analyze protein–protein interactions as described previously (Hudson et al., 2011). Briefly, pGBKT7- and pGADT7-based plasmids were co-transformed into the *Saccharomyces cerevisiae* PJ69–4a strain and selected on SD -Leu, -Trp plates. Drop tests were carried out on SD -Leu, -Trp, -His (with 0.1; 0.2; 0.3; 0.5; 1; 2; 3; 4; 5; 10; 15; 20; 30 mM 3-Amino-1,2,4-triazole; Sigma-Aldrich, USA) plates at 28°C. Each combination was co-transformed at least three times, and three independent drop tests were carried out.

### Pull-down assays

In a pull-down analysis examining the interaction of the PpNSE6 and PpNSE5 subunits (Figure 1d), T7-driven *in vitro* expression from plasmids pGBKT7-PpNSE5(aa190–526), pGBKT7-PpNSE5(aa245–526), and pET-Duet-PpNSE6(aa1–370)-StrepTwin-Stag was performed using the TNT kit (Promega, USA). Radiolabeled methionines (Met S<sup>35</sup>, Hartmann Analytic, Germany) were incorporated into the sequences of the synthesized proteins. Then, PpNSE5 proteins were mixed with PpNSE6 (input fraction) and preincubated at 4°C for 0.5 h in a total volume of 300 µL 1× phosphate buffer (10× phosphate buffer consisting of 42.9 mM Na<sub>2</sub>HPO<sub>4</sub>, 14.7 mM KH<sub>2</sub>PO<sub>4</sub>, 27 mM KCl, 1.37 M NaCl, 1% Tween-20, 0.02% sodium azide, pH 7.3). Mix was added to the protein-S beads (Millipore, USA) and incubated for 1.5 h at 4°C (unbound fraction taken). Beads were washed three times with 1× phosphate buffer, and proteins were released from beads with SDS buffer (bound fraction). Input, unbound, and bound fractions were separated by 12% SDS-PAGE, transferred to nitrocellulose membranes, and analyzed by phosphorimaging.

For the His-T7tag-PpNSE5 pull downs (Figures 2 and 3), pET28 constructs were transformed to BL21(DE3)RIL strain. Transformed bacteria were further inoculated and grown in liquid LB medium at 37°C to early exponential phase (OD<sub>600</sub> ~ 0.5). Expression was induced with 0.5 mM IPTG, and cultures were incubated at 37°C for 3–5 h. The harvested cells were resuspended in 1× phosphate buffer and sonicated with constant cooling on ice. Cleared lysates were incubated for 2 h on anti-T7-tag agarose beads (Millipore, USA) and washed three times with 1× phosphate buffer. Then, Met-S<sup>35</sup> radiolabeled proteins expressed *in vitro* [from pGADT7-PpSMC5(aa201–890), pGBKT7-PpSMC5(aa280–430 + 630–775), pGBKT7-PpSMC5(aa280–380 + 685–775), pGBKT7-PpSMC6(aa226–510 + 654–955), pGBKT7-PpSMC6(aa226–405 + 750–955), pGBKT7-PpSMC6(aa226–310 + 836–955) plasmids] were added (input fraction) and incubated overnight at 4°C in a total volume of 200 µL of 1× phosphate buffer (unbound fraction taken). Beads were washed three times with 1× phosphate buffer, and proteins were released from beads with SDS buffer (bound fraction). Input, unbound, and bound fractions were separated by 12% SDS-PAGE, transferred to nitrocellulose membranes, and analyzed by phosphorimaging and immunoblotting with the anti-T7tag HRP antibody (Abcam—ab19291, USA).

### In silico protein analysis

The PpNSE5 and PpNSE6 AlphaFold models from the EMBL-EBI database were used (Varadi et al., 2022). The rod-like PpSMC5 and PpSMC6 structural models were generated with the Swiss-Model tool using 7QCD cryoEM structures as templates (Hallett et al., 2022; Schwede et al., 2003). The headless PpSMC5 and PpSMC6 fragments were modeled using the AlphaFold/ColabFold tool (Mirdita et al., 2022). Secondary structure and fragment borders were determined based on the 3D models. The structures were aligned and visualized using the PyMOL software (Schrodinger Inc., USA).

### Plant material cultivation and analysis

The wild-type *P. patens*, accession (Hedw.) B.S.G. (Rensing et al., 2008), was utilized to create the *Ppnse5* mutants. The moss lines were cultivated either as ‘spot inocula’ on BCD agar medium enriched with 1 mM CaCl<sub>2</sub> and 5 mM ammonium tartrate (BCDAT medium) or as lawns of protonema filaments by subculturing homogenized tissue on BCDAT agar, overlaid with cellophane, within growth chambers maintained at an 18/6-h day/night cycle and a temperature of 22/18°C (Cove et al., 2009). In dark conditions, 0.5% sucrose was included in the medium, and 1.5% agar was used. Petri dishes were positioned vertically to enhance the observation of caulonema growth.

The growth rates were determined by weighing untreated explants of mutant lines and comparing them with untreated explants of WT. Sensitivity to DNA damage was measured as described previously (Lelkes et al., 2023). Protocols for DNA isolation and rDNA copy numbers analysis were also detailed in Lelkes et al. (2023).

The pictures of whole colonies were taken by Canon EOS77D, objective Canon EF 28–135 mm f/3.5–5.6. The details of gametophores were photographed by Stereomicroscope Leica M205FA, objective Plan-Apochromat 2.0x. Staining with 10 µg/mL propidium iodide (PI, Sigma-Aldrich) was performed as described previously (Lelkes et al., 2023).

### Construction of *Ppnse5* mutant lines

The STOP codon knock-in was achieved through homology-directed repair following the induction of double-strand breaks (DSB) within the *PpNSE5* locus by Cas9. We used two double-stranded DNA donor templates, one 45 bp and the other 40 bp in length, to introduce the desired mutations for constructing *Ppnse5KO1* and *Ppnse5KO2*, respectively. These donor templates were synthesized as pairs of complementary oligonucleotides (pKA1390 and pKA1391 for *Ppnse5KO1*; pKA1394 and pKA1395 for *Ppnse5KO2*; Table S2) designed to be homologous to the first and fifth exons of the *PpNSE5* locus (Figure 4a). The *Ppnse5KO1* template contained a +40CCT to TAG substitution (resulting in a STOP codon at the 14th amino acid position) and a +55A to C substitution, which generated a *Bsa*I cleavage site. The *Ppnse5KO2* template featured a +1236A to T substitution (resulting in a STOP codon at the 168th amino acid position) and a +1253A to C substitution, creating a *Sa*II cleavage site.

We utilized the Gateway destination vector pMK-Cas9 (Addgene plasmid #113743) containing the Cas9 expression cassette and kanamycin resistance marker, along with the entry vector pENTR-PpU6sgRNA-L1L2 (Addgene plasmid #113735), which harbored the PpU6 promoter and sgRNA scaffold, as previously described (Mallett et al., 2019). PpNSE5-specific sgRNA spacers were synthesized as pairs of complementary oligonucleotides (pKA1392 + pKA1393 for *Ppnse5KO1* and pKA1396 + pKA1397 for



*Ppnse5KO2*; Table S2). We added four nucleotides to the 5'-ends of these oligonucleotides to create sticky ends compatible with *Bsal*-linearized pENTR-PpU6sgRNA-L1L2. The Cas9/sgRNA expression vectors were generated using the Gateway LR reaction, recombining the entry vector with the *Ppnse5* sgRNA spacers and the destination vector.

These DNA constructs, together with the appropriate donor templates (annealed pKA1390 + pKA1391 for *Ppnse5KO1* or pKA1394 + pKA1395 for *Ppnse5KO2*), were co-transformed into protoplasts via PEG-mediated transformation. All sgRNAs were designed in the CRISPOR online software using *P. patens* (Phytozome V11) and *S. pyogenes* (5' NGG 3') as the genome and PAM parameters, respectively. The protospacers with the highest specificity score were chosen.

After 5 days of regeneration, the transformed protoplasts were transferred to the BCDAT medium supplemented with 50 µg/mL G418 for selection. Following 1 week of selection, the G418-resistant lines were propagated. Crude extracts from young tissues of these lines were used for PCR amplification of genomic DNA surrounding the editing sites, employing primers pKA1437 + pKA1438 for *Ppnse5KO1* and pKA1439 + pKA1440 for *Ppnse5KO2*. The resulting PCR products were cleaved using *Bsal* or *SalI* and subjected to DNA electrophoresis. Lines for which the PCR product was successfully cleaved underwent sequencing to confirm the accurate introduction of mutations.

We identified two lines, *Ppnse5KO1-16* and *Ppnse5KO1-23*, with correctly integrated STOP codons in the first exon and two lines, *Ppnse5KO2-14* and *Ppnse5KO2-21*, with accurately incorporated STOP codons in the fifth exon. Both mutants of the respective mutation exhibited similar morphology and growth responses to bleomycin treatment. We chose the *Ppnse5KO1-16* and *Ppnse5KO2-14* lines for further experiments with a slightly more pronounced phenotype.

### Evaluation of the frequency of spontaneous mutations

The frequency of spontaneous mutations was assessed using the adenine phosphoribosyl transferase (*APT*) gene reporter system (Trouiller et al., 2006). Loss of function in the *APT* gene confers resistance to a toxic adenine analogue known as 2-fluoro adenine (2-FA). To evaluate this phenotype, tissue samples from 7-day-old WT and mutant lines were homogenized and then incubated in 10 mL of liquid BCDAT medium for 24 h to facilitate recovery. Subsequently, 1 mL of the homogenized tissue was used to determine the dry tissue weight, while the remaining tissue was planted onto BCDAT medium supplemented with 5 µM 2-FA. After 3 weeks of incubation, the number of the 2-FA resistant colonies was counted. The frequency of spontaneous mutagenesis is given as the number of 2-FA resistant colonies per mg of dry tissue. The experiments were repeated four times.

### AUTHOR CONTRIBUTIONS

*Conceptualization, supervision, and funding acquisition:* JJP, KJA, BŠ; *Data curation and formal analysis:* JJP, JV, EL, KJA, MH; *Investigation:* JV, MH, EL, RV, BŠ, BK; *Visualization:* JJP, JV, KJA, MH; *Writing—original draft and revision preparation:* JJP, KJA, MH, JV.

### ACKNOWLEDGEMENTS

We acknowledge the Imaging Facility of the Institute of Experimental Botany AS CR, supported by the MEYS CR (LM2018129 Czech-Biolmaging). Open access publishing facilitated by Masarykova univerzita, as part of the Wiley - CzechELib agreement.

### FUNDING INFORMATION

Funding from the Czech Science Foundation (CSF project GA20-05095S) to J.J.P and K.J.A is gratefully acknowledged. B.Š. received a Career restart grant from Masaryk University (MUNI/R/1142/2021).

### CONFLICT OF INTEREST STATEMENT

The authors declare no conflict of interest.

### DATA AVAILABILITY STATEMENT

All the data are available in the main paper or online Supporting information.

### SUPPORTING INFORMATION

Additional Supporting Information may be found in the online version of this article.

**Methods S1.** Supplementary methods.

**Figure S1.** PpNSE5 protein analysis.

**Figure S2.** PpSMC6 analysis.

**Figure S3.** PpSMC5 analysis.

**Figure S4.** Characterization of the moss *Ppnse5* mutants.

**Table S1.** List of cloning primers.

**Table S2.** Primers for moss analysis and manipulation.

### REFERENCES

- Adamus, M., Lelkes, E., Potesil, D., Ganji, S.R., Kolesar, P., Zabradý, K. et al. (2020) Molecular insights into the architecture of the human SMC5/6 complex. *Journal of Molecular Biology*, **432**, 3820–3837.
- Alt, A., Dang, H.Q., Wells, O.S., Polo, L.M., Smith, M.A., McGregor, G.A. et al. (2017) Specialized interfaces of SMC5/6 control hinge stability and DNA association. *Nature Communications*, **8**, 14011.
- Aragón, L. (2018) The SMC5/6 complex: new and old functions of the enigmatic long-distance relative. *Annual Review of Genetics*, **52**, 89–107.
- Bürmann, F. & Löwe, J. (2023) Structural biology of SMC complexes across the tree of life. *Current Opinion in Structural Biology*, **80**, 102598.
- Collier, J.E., Lee, B.G., Roig, M.B., Yatskevich, S., Petela, N.J., Metson, J. et al. (2020) Transport of DNA within cohesin involves clamping on top of engaged heads by Scc2 and entrapment within the ring by Scc3. *eLife*, **9**, e59560.
- Collier, J.E. & Nasmyth, K.A. (2022) DNA passes through cohesin's hinge as well as its SMC3-kleisin interface. *eLife*, **11**, e80310.
- Cove, D.J., Perroud, P.F., Charron, A.J., McDaniel, S.F., Khandelwal, A. & Quatrano, R.S. (2009) The moss *Physcomitrella patens*: a novel model system for plant development and genomic studies. *Cold Spring Harbor Protocols*, **2009**, pdb.em0115.
- Cove, D.J., Schild, A., Ashton, N.W. & Hartmann, E. (1978) Genetic and physiological studies of the effect of light on the development of the moss, *Physcomitrella patens*. *Photochemistry and Photobiology*, **27**, 249–254.
- Davidson, I.F., Bauer, B., Goetz, D., Tang, W., Wutz, G. & Peters, J.M. (2019) DNA loop extrusion by human cohesin. *Science*, **366**, 1338–1345.
- Davidson, I.F. & Peters, J.M. (2021) Genome folding through loop extrusion by SMC complexes. *Nature Reviews Molecular Cell Biology*, **22**, 445–464.
- Duan, X., Yang, Y., Chen, Y.H., Arenz, J., Rang, G.K., Zhao, X. et al. (2009) Architecture of the SMC5/6 complex of *Saccharomyces cerevisiae* reveals a unique interaction between the Nse5-6 subcomplex and the hinge regions of SMC5 and SMC6. *The Journal of Biological Chemistry*, **284**, 8507–8515.
- Ganji, M., Shaltiel, I.A., Bisht, S., Kim, E., Kalichava, A., Haering, C.H. et al. (2018) Real-time imaging of DNA loop extrusion by condensin. *Science*, **360**, 102–105.
- Gutierrez-Escribano, P., Hormeno, S., Madariaga-Marcos, J., Sole-Soler, R., O'Reilly, F.J., Morris, K. et al. (2020) Purified SMC5/6 complex exhibits



- DNA substrate recognition and compaction. *Molecular Cell*, **80**, 1039–1054.
- Hallett, S.T., Campbell Harry, I., Schellenberger, P., Zhou, L., Cronin, N.B., Baxter, J. *et al.* (2022) Cryo-EM structure of the Smc5/6 holo-complex. *Nucleic Acids Research*, **50**, 9505–9520.
- Hassler, M., Shaltiel, I.A. & Haering, C.H. (2018) Towards a unified model of SMC complex function. *Current Biology*, **28**, R1266–R1281.
- Higashi, T.L., Pobegalov, G., Tang, M., Molodtsov, M.I. & Uhlmann, F. (2021) A Brownian ratchet model for DNA loop extrusion by the cohesin complex. *eLife*, **10**, e67530.
- Holá, M., Vágnerová, R. & Angelis, K.J. (2021) Kleisin NSE4 of the SMC5/6 complex is necessary for DNA double strand break repair, but not for recovery from DNA damage in *Physcomitrella* (*Physcomitrium patens*). *Plant Molecular Biology*, **107**, 355–364.
- Hudson, J.J.R., Bednarova, K., Kozakova, L., Liao, C.Y., Guerineau, M., Colnaghi, R. *et al.* (2011) Interactions between the Nse3 and Nse4 components of the SMC5-6 complex identify evolutionarily conserved interactions between MAGE and EID families. *PLoS One*, **6**, 14.
- Lee, B.G., Merkel, F., Allegretti, M., Hassler, M., Cawood, C., Lecomte, L. *et al.* (2020) Cryo-EM structures of holo condensin reveal a subunit flip-flop mechanism. *Nature Structural & Molecular Biology*, **27**, 743–751.
- Lelkes, E., Jemelkova, J., Holá, M., Stefanovie, B., Kolesar, P., Vagnerova, R. *et al.* (2023) Characterization of the conserved features of the NSE6 subunit of the *Physcomitrium patens* SMC5/6 complex. *Plant Journal*, **115**, 1084–1099.
- Li, S., Yu, Y., Zheng, J., Miller-Browne, V., Ser, Z., Kuang, H. *et al.* (2023) Molecular basis for Nse5-6 mediated regulation of Smc5/6 functions. *Proceedings of the National Academy of Sciences of the United States of America*, **120**, e2310924120.
- Li, X., Liu, K., Li, F., Wang, J., Huang, H., Wu, J. *et al.* (2012) Structure of C-terminal tandem BRCT repeats of Rtt107 protein reveals critical role in interaction with phosphorylated histone H2A during DNA damage repair. *The Journal of Biological Chemistry*, **287**, 9137–9146.
- Mahrik, L., Stefanovie, B., Maresova, A., Princova, J., Kolesar, P., Lelkes, E. *et al.* (2023) The SAGA histone acetyltransferase module targets SMC5/6 to specific genes. *Epigenetics & Chromatin*, **16**, 6.
- Mallett, D.R., Chang, M., Cheng, X. & Bezanilla, M. (2019) Efficient and modular CRISPR-Cas9 vector system for *Physcomitrella patens*. *Plant Direct*, **3**, e00168.
- Mirdita, M., Schütze, K., Moriwaki, Y., Heo, L., Ovchinnikov, S. & Steinegger, M. (2022) ColabFold: making protein folding accessible to all. *Nature Methods*, **19**, 679–682.
- Oravcová, M. & Boddy, M.N. (2019) Recruitment, loading, and activation of the Smc5–Smc6 SUMO ligase. *Current Genetics*, **65**, 669–676.
- Oravcova, M., Nie, M.H., Zilio, N., Maeda, S., Jami-Alahmadi, Y., Lazzerini-Denchi, E. *et al.* (2022) The Nse5/6-like SIMC1-SLF2 complex localizes SMC5/6 to viral replication centers. *eLife*, **11**, 37.
- Palecek, J., Vidot, S., Feng, M., Doherty, A.J. & Lehmann, A.R. (2006) The SMC5-6 DNA repair complex: bridging of the SMC5-6 heads by the Kleisin, NSE4, and non-Kleisin subunits. *The Journal of Biological Chemistry*, **281**, 36952–36959.
- Palecek, J.J. (2019) SMC5/6: multifunctional player in replication. *Genes*, **10**, E7.
- Palecek, J.J. & Gruber, S. (2015) Kite proteins: a superfamily of SMC/Kleisin partners conserved across bacteria, archaea, and eukaryotes. *Structure*, **23**, 2183–2190.
- Peng, X.P., Lim, S., Li, S.B., Marjavaara, L., Chabes, A. & Zhao, X.L. (2018) Acute Smc5/6 depletion reveals its primary role in rDNA replication by restraining recombination at fork pausing sites. *PLoS Genetics*, **14**, 20.
- Petela, N.J., Gonzalez Llamazares, A., Dixon, S., Hu, B., Lee, B.G., Metson, J. *et al.* (2021) Folding of cohesin's coiled coil is important for Scc2/4-induced association with chromosomes. *eLife*, **10**, e67268.
- Pradhan, B., Kanno, T., Umeda Igarashi, M., Loke, M.S., Baaske, M.D., Wong, J.S.K. *et al.* (2023) The Smc5/6 complex is a DNA loop-extruding motor. *Nature*, **616**, 843–848.
- Räschle, M., Smeenk, G., Hansen, R.K., Temu, T., Oka, Y., Hein, M.Y. *et al.* (2015) DNA repair. Proteomics reveals dynamic assembly of repair complexes during bypass of DNA cross-links. *Science*, **348**, 1253671.
- Rensing, S.A., Lang, D., Zimmer, A.D., Terry, A., Salamov, A., Shapiro, H. *et al.* (2008) The *Physcomitrella* genome reveals evolutionary insights into the conquest of land by plants. *Science*, **319**, 64–69.
- Schwede, T., Kopp, J., Guex, N. & Peitsch, M.C. (2003) SWISS-MODEL: an automated protein homology-modeling server. *Nucleic Acids Research*, **31**, 3381–3385.
- Sergeant, J., Taylor, E., Palecek, J., Fouteri, M., Andrews, E., Sweeney, S. *et al.* (2005) Composition and architecture of the *Schizosaccharomyces pombe* Rad18 (Smc5-6) complex. *Molecular and Cellular Biology*, **25**, 172–184.
- Shi, Z.B., Gao, H.S., Bai, X.C. & Yu, H.T. (2020) Cryo-EM structure of the human cohesin-NIPBL-DNA complex. *Science*, **368**, 1454–1459.
- Taschner, M., Basquin, J., Steigenberger, B., Schafer, I.B., Soh, Y.M., Basquin, C. *et al.* (2021) Nse5/6 inhibits the Smc5/6 ATPase and modulates DNA substrate binding. *EMBO Journal*, **40**, 23.
- Torres-Rosell, J., Sunjevaric, I., De Piccoli, G., Sacher, M., Eckert-Boulet, N., Reid, R. *et al.* (2007) The Smc5–Smc6 complex and SUMO modification of Rad52 regulates recombinational repair at the ribosomal gene locus. *Nature Cell Biology*, **9**, 923–931.
- Trouiller, B., Schaefer, D.G., Charlot, F. & Nogué, F. (2006) MSH2 is essential for the preservation of genome integrity and prevents homeologous recombination in the moss *Physcomitrella patens*. *Nucleic Acids Research*, **34**, 232–242.
- Uhlmann, F. (2016) SMC complexes: from DNA to chromosomes. *Nature Reviews. Molecular Cell Biology*, **17**, 399–412.
- Varadi, M., Anyango, S., Deshpande, M., Nair, S., Natassia, C., Yordanova, G. *et al.* (2022) AlphaFold Protein Structure Database: massively expanding the structural coverage of protein-sequence space with high-accuracy models. *Nucleic Acids Research*, **50**, D439–D444.
- Vondrova, L., Kolesar, P., Adamus, M., Nociar, M., Oliver, A.W. & Palecek, J.J. (2020) A role of the Nse4 kleisin and Nse1/Nse3 KITE subunits in the ATPase cycle of SMC5/6. *Scientific Reports*, **10**, 13.
- Williams, J.S., Williams, R.S., Dovey, C.L., Guenther, G., Tainer, J.A. & Russell, P. (2010) gammaH2A binds Brc1 to maintain genome integrity during S-phase. *The EMBO Journal*, **29**, 1136–1148.
- Yu, Y., Li, S., Ser, Z., Kuang, H., Than, T., Guan, D. *et al.* (2022) Cryo-EM structure of DNA-bound Smc5/6 reveals DNA clamping enabled by multi-subunit conformational changes. *Proceedings of the National Academy of Sciences of the United States of America*, **119**, e2202799119.
- Yu, Y., Li, S.B., Ser, Z., Sanyal, T., Choi, K., Wan, B.B. *et al.* (2021) Integrative analysis reveals unique structural and functional features of the Smc5/6 complex. *Proceedings of the National Academy of Sciences of the United States of America*, **118**, 11.
- Zabradny, K., Adamus, M., Vondrova, L., Liao, C., Skoupilova, H., Novakova, M. *et al.* (2016) Chromatin association of the SMC5/6 complex is dependent on binding of its NSE3 subunit to DNA. *Nucleic Acids Research*, **44**, 1064–1079.